3D In-situ Stop Action Study of Recrystallization in Additively Manufactured 316L Stainless Steel: Reconstruction Optimization and Observations

3D In-situ Stop Action Study of Recrystallization in Additively Manufactured 316L Stainless Steel: Reconstruction Optimization and Observations

H Liu[1], Y Zhang[2], M Wilkin[2], J-S Park[3], P Kenesei[3], A D Rollett[2] and R M Suter[1]

[1] Department of Physics, Carnegie Mellon University, Pittsburgh, PA 15213, USA
[2] Department of Materials Science and Engineering, Carnegie Mellon University, Pittsburgh, PA 15213, USA
[3] X-ray Science Division, Argonne National Laboratory, Lemont, IL 60439 USA

E-mail: suter@andrew.cmu.edu

Abstract. A volume of an additively manufactured 316L stainless steel sample has been tracked during its recrystallization using near- and far-field High Energy Diffraction Microscopy (HEDM) and absorption tomography at Advanced Photon Source beamline 1-ID. A near-field compatible *in situ* furnace allows monitoring of Bragg diffraction signals as they evolve out of a weak and diffuse background while the sample temperature is $\approx$ 1250° C. The sample is rapidly cooled to room temperature after observation of significant signal evolution and $\sim 0.035\,\mathrm{mm}^3$ is mapped by the near-field method. Four cycles of heat treatment follow the structure from a state of small, isolated grains through impingement of domains to near completion of recyrstallization. Here, the experiment and reconstructions are described, and recrystallized fractions, twin domains, and distributions of grain boundary types are discussed.

1. Introduction

Additive manufacturing (AM) facilitates the rapid manufacture of precision parts in small numbers and made with unusual materials with a drastically abbreviated design-to-production process. Despite the obvious advantages of AM, there are many open questions that deserve attention from the research community. For example, the laser melting and subsequent re-solidification occur orders of magnitude faster than in conventional materials processing and this changes many aspects of the processing-microstructure-properties-performance relationships. [1, 2] Standard aids for processing such as time-temperature-transformation diagrams are no longer valid. Different grain structures, segregation patterns and precipitate structures are obtained, all of which change the material properties and, especially with metals, how the material responds to subsequent heat treatment. [3] Stored defects and consequent stresses can lead to degradation of mechanical properties. Post-build thermal processes have been developed to relieve these stresses. [4]

Here, the heat treatment of a laser powder bed AM sample of 316L stainless steel is investigated. Recrystallization is observed in real time as the sample is heated to $\approx$ 1250°C while mounted for High Energy Diffraction Microscopy (HEDM) measurements at the 1-ID beamline of the Advanced Photon Source (APS) at Argonne National Laboratory. Near-field

HEDM is used to map recrystallized grain unit cell orientations in a measured volume of $V_m = 0.5 \times 0.5 \times 0.14$ mm^3 $= 0.035$ mm^3. Over four annealing cycles, the sample evolves from a sparse distribution of small, almost randomly oriented, isolated grains to being almost fully recrystallized and filling the measured volume with well ordered grains. The material maintains its face centered cubic crystal structure and this gives rise to extensive twinning with twin-related domains containing up to 20 individual crystals. The final structure is dominated by domains that arose in the first annealing cycle resulting in at most weak recrystallization texture.

2. Procedures

A nf-HEDM compatible *in situ* furnace, developed for these measurements, is shown in figure 1. The system is similar to one currently in use at CHESS. [5] Infrared radiation from two lamps is focused on the sample position and allows rapid heating and cooling. There is no mechanical contact between the furnace and sample. Forming gas (97% N_2, 3%H_2) circulates through the sample chamber to prevent oxidation and cooling water keeps the furnace body close to ambient temperature. To monitor the progress of recrystallization, repeated measurements of near-field diffraction signals integrated over the same 30° interval are carried out with the detector placed as shown. This brings the scintillator to ~ 12 mm from the sample rotation axis. Any illuminated crystalline grain should contribute diffraction in this rotation range. Upon observing subtle but significant changes in the signal, the furnace is turned off and removed and room temperature HEDM and tomography measurements are performed. The sample volume of interest was measured in four states referred to as annealing cycles 1 through 4. Annealing between each state used $T = 1250$°C which was found to generate dynamics that were visible on detector images within a few minutes.

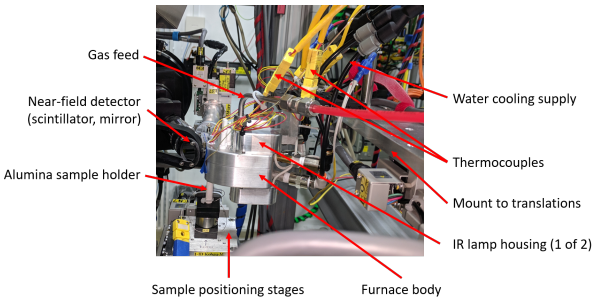

Figure 1: The fully instrumented *in situ* furnace installed at the 1-ID beamline at the APS. The aluminum bar at right holds the furnace and is connected to XYZ translations stages that position the furnace over the sample or remove it for room temperature measurements.

Figure 2 shows the evolution of near-field detector signal over the first three annealing cycles. Initially, from the as-built material, the signal is weak and dispersed with few if any Bragg-like peaks. This indicates that the material is in a deformed state (EBSD measurements are being performed on as built material). In successive annealed states, sharp peaks emerge and grow in size and number.

Microstructure cross-sections are obtained from 1440 images collected at two rotation-axis-to-detector distances (deduced to be $L = 5.614$ and 7.614 mm) integrated over $\delta\omega = 0.25$° intervals and spanning 180° sample rotation. Standard image analysis is performed on the detector images; this subtracts a median background image which largely eliminates broad, signals from unrecrystallized material, and then extracts sharp signals using the Laplacian of Gaussian "blob" finding algorithm. [6]

Reconstructions of recrystallized grains used the HEXOMAP package (available here on GitHub). This is a python/pyCUDA based GPU accelerated code based on the forward modeling C++ routines from well proven previous generation code. [7, 8] In contrast to the old code, reconstructions are performed on a square array of sample *points* rather than triangular area elements; this makes reconstructions more efficient (fewer redundant projections) and makes importing deduced structures into graphics and modeling codes considerably more straightforward. The volume associated with each reconstruction point is still referred to as a

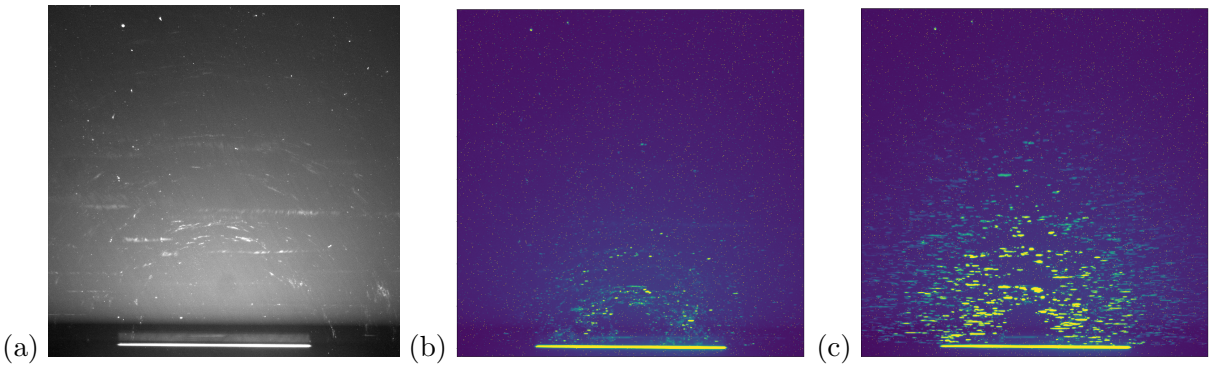

Figure 2: nf-HEDM signal evolution with annealing treatment. (a) Raw image from as-built material with no background subtraction. (b) Background subtracted, integrated image collected while the sample rotated through 30° in the cycle 1 state. (c) Same as (b) but after annealing cycle 3. The clear emergence of sharp Bragg diffraction spots is associated with the growth of recrystallized domains. The bright horizontal line at bottom is the attenuated incident beam. The detector has a 3×3 mm field-of-view.

"voxel;" in the current case, the point mesh has spacings $2 \times 2 \times 4$ μm^3, with the last value being the spacing between layer measurements. For a given unit cell orientation and sample position or voxel, the forward model code projects diffracted beams to a simulated detector space and looks for the orientation that generates maximal overlap with the experimental binarized detector pattern. The overlap is measured by a confidence or completeness parameter, $\mathcal{C}$, which is the fraction of simulated Bragg peaks that strike experimentally observed intensity. The ease of code modification and extension in the python environment allows development of special purpose routines; two such routines were developed in this work and are available for general use:

Boundary position optimization. To accelerate reconstructions, a "flood fill" algorithm is used in which a found orientation is tried as an initial guess for neighboring voxels to avoid *ab initio* searches over the entire zone of possible orientations for each voxel. The found orientation (with local Monte Carlo tweaking) can fill in an entire grain cross-section. However, this has the danger of dilating some grains at the expense of neighbors. To address this, a post-processing algorithm tests all orientations in the neighborhood of a boundary and switches orientations if $\mathcal{C}$ increases. Iterations continue until no further changes are made. The small number of test orientations makes this optimization fast.

Twin checking. Small twinned regions generate diffraction signals that are small and potentially weak; more extended parent generated signals may extend into the domain of the twin. By testing all twin variant orientations at each voxel location, weak signals may be found in the detector data. Any increase in $\mathcal{C}$ or reduction to within a given threshold can be kept as an existing twin. Again, the small number of test orientations makes this fast. This algorithm was applied here for the FCC twinning case but additional twin variant sets can be generated easily for other cases.

3. Results

Figure 3 shows the evolution of microstructure in a single layer; this layer is in the center of the measured volume which implies that most of the observed grains occur in neighboring layer measurements as well. Close inspection reveals that many of the grains that appear in (a) persist and grow in later cycles. In later states, there are additional small grains that appear and

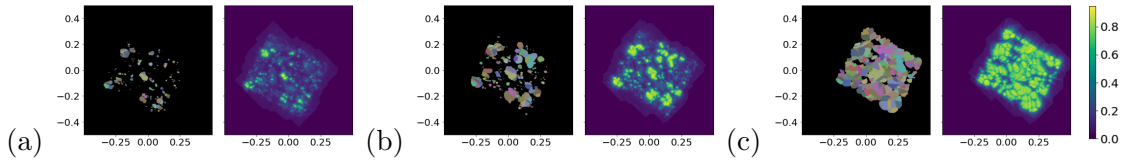

Figure 3: A single cross-section of microstructure after (a) Cycle 1, (b) Cycle 2, (c) Cycle 3 *in situ* annealing treatments. Scale markings are in millimeters. This is layer 17 of the 33 measured. In each case, the color coded orientation map (colors scaled to RGB weights from Rodrigues vector components) is on the left and the confidence parameter, $\mathcal{C}$, is on the right. Note that these images have not been mutually registered, so one can see that the sample did not always return to precisely the same position after heating. The vertical positions of layer measurements were referenced to the top of the sample after each annealing, so should be repeatable to ~ 1 μm.

there are grains that appeared first in other cycles and grew into the layer shown. In addition, some grains that appear in one state are consumed by others through the coarsening process. The maps of $\mathcal{C}$ show the clear contrast between recrystallized ($\mathcal{C} > 0.4$) and unrecrystallized material ($\mathcal{C} < 0.4$). Orientation maps are thresholded to show only voxels with $\mathcal{C} > 0.4$. The smallest grains have reduced values of $\mathcal{C}$ compared to larger grains due to the reduced amount of crystal volume that projects into individual detector pixels and consequent reduced peak intensities, reduced precision in peak shape determination, and more simulated peaks that miss the segmented peaks in the data set. Note, on the other hand, the large dynamic range of the measurement: the smallest grain cross-sections are ~ 16 μm^2 and the largest are $\sim 2\times10^4$ μm^2.

The recrystallized grains show resolution limited intra-granular orientation variations, i.e., < 0.1 degree disorientations indicating a high degree of crystalline order and low defect density as observed in recrystallization of more conventionally deformed materials.

Before addressing the details of observed microstructure, the elucidation of which is the motivation for this work, what do the data say about global aspects of recrystallization dynamics? Table 1 shows the progress of recrystallization over the four annealing cycles including anneal times and the fraction of recrystallized volume, $X(t)$, calculated as the measured volume with $\mathcal{C} > 0.35$ in each state divided by the total measured volume, V_m. The time is the duration in seconds of annealing at $T_a = 1250$°C. The Johnson-Mehl-Avrami-Kolmogorov equation [9], which can be written as

Table 1: Recrystallized volume fractions.

	Time (s)	$X(t)$
Cycle 1	57	0.061
Cycle 2	53	0.201
Cycle 3	150	0.474
Cycle 4*	306	0.915

*Cycle 4 annealing and measurement were performed separately from others and involved removing and remounting the sample.

$$X(t) = 1 - e^{-(t/\tau)^n}, \tag{1}$$

with n a dimensionless exponent expected to be close to three in three dimensions and with nucleation from random sites, [9] and τ is a characteristic time scale where $X(\tau) = 1 - e^{-1} = 0.632$. This equation was proposed as a means to capture two phases of the progression of recrystallization: first, grains nucleate and grow quickly into unrecrystallized deformed material driven by the energy release in crystallization; when domains impinge on each other, growth slows since a large fraction of the advancing fronts are pinned against previously recrystallized material. Of course, the newly formed grain boundaries can continue to migrate to reduce boundary energy, but this has no effect on X. If a simple equation of the form of (1) can be validated and shown to be general, it could be useful for process design in a wide range of contexts. Measurements such as this one present an opportunity to test such expressions.

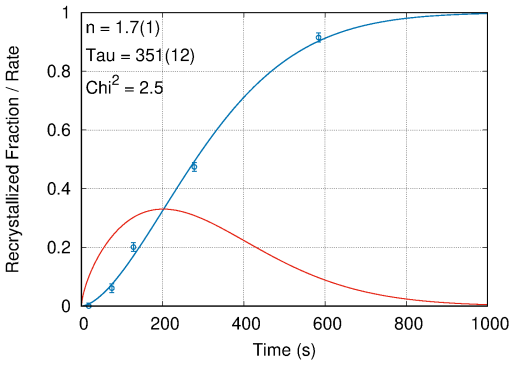

Figure 4: Non-linear least squares fit of the data in Table 1 to (1). The red curve is 150 times the time derivative of (1), giving the recrystallization rate.

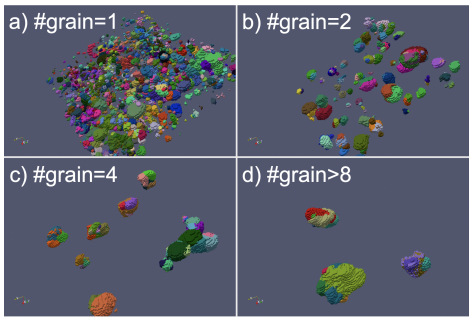

Figure 5: Twin related domains (TRDs) present after annealing cycle 2. Each panel shows only those TRDs composed of (a) 1, (b) 2, (c) 4, and (d) 8 or more twin related grains.

Figure 4 shows a weighted non-linear least squares fit [10] to (1) which results in $n = 1.7(1), \tau = 351(12)$ s, with "(...)" being the uncertainty in the previous digit, and $\chi^2 = 2.5$. Error bars on the X were approximated from sensitivities to variations in the $\mathcal{C}$ threshold (strictly, such variations give rise to systematic uncertainty rather than the desired random measurement noise). While the exponent is almost consistent with $n = 2$, the result is clearly inconsistent with $n = 3$. However, as an empirical representation of the data the result is quite good. The rate curve in figure 4 shows the expected behavior with zero rate at $t = 0$, as initial nuclei begin to yield growing crystals, followed by rapid growth and a long tail of slower growth as completion is approached. This fitting exercise is demonstrative but is not robust enough to rigorously support or refute the validity of (1): The values of n and τ have a substantial correlation coefficient of -0.3 and, with only four data points, the data do not clearly define the shape of $X(t)$. Further, while this fit included a data point at $X(18\text{ s}) = 0$ (the result of a brief test heating), the definition of $t = 0$ is unclear and may have a strong effect on the deduced exponent. The reduced value of n may reflect the complexity of growth paths seen in [11] .

Now turning to the grain scale, figure 5 shows three dimensional views of twin related domains (TRD) after two cycles of annealing. No smoothing has been applied to the grain shapes, so the voxels are shown as $2 \times 2 \times 4$ μm^3 boxes which correspond to the reconstruction point spacings. Most grains are not twinned ($\#grain = 1$) but many TRDs contain multiple twins and these numbers grow with further annealing. By cycle 3, the V_m is largely filled with TRDs; domains have as many as 20 twin related grain members, many of which necessarily have the same orientation (given only four twin variant choices) but are not in contact with each other. Multiple examples can be seen in figure 5 in which TRDs contain three and four distinct orientations, some with disconnected grains with the same orientation.

Figure 6 shows the fractional population of different classes of grain boundaries in each measured annealing cycle. Each class is specified by the three parameter disorientation between adjoining grains, so all boundary orientations (relative to the adjoining crystal unit cells) are included in each class. The large fraction of $\Sigma 3$ boundaries (red) (disorientation of 60° about a (111) axis) reflects the extent of twinning in the recrystallization microstructure of this FCC material; this single disorientation represents about 40% of all boundaries. The $\Sigma 9$ boundaries (orange) occur at intersections at triple lines involving two twin boundaries. A small number of general boundaries are found within the TRDs (green), reflecting intersections involving at least one non-(111) surface. Just over 60% of disorientations are general boundary types that form through impingement between independent TRDs (red) which have essentially random

orientations.

4. Conclusion and future work

This brief article has focused on technical developments that were necessary to perform one of the first *in situ* grain mapped measurements in three dimensions of recrystallization and on two examples of unique information extracted. Improvements have been made in the algorithms used to optimize reconstructions of orientation maps making them both fast and accurate and more sensitive to subtle features such as crystallographic twins. [12] It is only with nf-HEDM and analogous high energy x-ray methods that it is possible to gather the statistics to image evolution of material as in figure 5. The procedures applied here can be used in future studies of microstructure evolution processes.

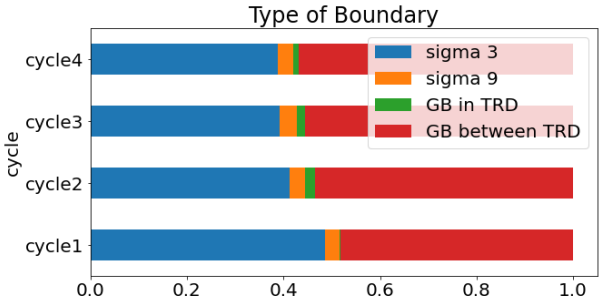

Figure 6: Fractions of grain boundary classes during recrystallization of AM 316L stainless steel.

Further studies are needed to determine the generality of the above observations. It would be interesting to compare recrystallization of AM processed 316L to conventional roll-deformed metals, including 316L, other steels and beyond. For example, in this work it is seen that grains that grew out of deformed material in annealing cycle 1 come to dominate the final microstructure. Grains that appear later tend to be consumed due to their small size by the larger cycle 1 grains. Presumably, by controlling the density of cycle 1 grains, one may be able to tailor the final microstructure to be more like that of conventional wrought material which has a smaller grain size than that seen here.

Acknowledgments

The authors thank F. Wagner for informative discussions. This work was supported by the U.S. Department of Energy under NNSA Award DE-NA0003915. This research used resources of the Advanced Photon Source, a U.S. Department of Energy Office of Science user facility at Argonne National Laboratory and is based on research supported by the U.S. DOE Office of Science-Basic Energy Sciences, under contract DE-AC02-06CH11357.

References

[1] Oh S A, Lim R E, Aroh J W, Chuang A C, Gould B J, Bernier J V, Parab N, Sun T, Suter R M and Rollett A D 2021 *JOM* **73** 212–22
[2] Oh S A, Lim R E, Aroh J W, Chuang A C, Gould B J, Amin-Ahmadi B, Bernier J V, Sun T, Pistorius P C, Suter R M and Rollett A D 2021 *Mat. Res. Lett.* **9** 429–36
[3] Zhang F, Levine L E, Allen A J, Stoudt M R, Lindwall G, Lass E A, Williams M E, Idell Y and Campbell C E 2018 *Acta Mat.* **152** 200–14
[4] Pokharel R, Patra A, Brown D W, Clausen B, Vogel S C and Gray G T 2019 *I. J. Plast.* **121** 201–17
[5] Pagan D C, Bernier J V, Dale D, Ko J Y P, Turner T J, Blank B and Shade P A 2018 *Scripta Mat.* **142** 96–100
[6] Lind J, Rollett A, Pokharel R, Hefferan C, Li S and U Lienert R S 2014 IEEE Int. Conf. Image Proc. pp 4877–81
[7] Li S and Suter R 2013 *J. Appl. Cryst.* **46** 512–24
[8] Menasche D, Shade P and Suter R 2020 *J. Appl. Cryst.* **53** 107–16
[9] Humphreys J, Rohrer G and Rollett A 2017 *Recrystallization and Related Annealing Phenomena, Third Edition* (Amsterdam, Netherlands: Elsevier)
[10] Bevington D K and Robinson P R 1992 *Data Reduction and Error Analysis for the Physical Sciences* 2nd ed (McGraw-Hill) ISBN 978-0072472271
[11] Lauridsen E, Poulsen H, Nielsen S and Jensen D J 2003 *Acta Mat.* **51** 4423–35
[12] For HEXOMAP and associated analysis codes, much of which was developed by co-author He Liu for this work, see https://github.com/HeLiuCMU/HEXOMAP.